

Numerical modelling of unsteady 2D sheet cavitation

par D.F. De Lange, G.J. De Bruin, L. Van Wijngaarden

University of Twente (Enschede, The Netherlands)

I ■ INTRODUCTION

In unsteady sheet cavitation on ship propellers it has been observed, that a cavity sheet can be shed off partly or completely and develop into a cloud on the afterbody of the propeller, where a collective collapse of the bubbles within that cloud can happen [1, 2, 3]. A complete break-off cycle (fig. 1 and 2) is described by :

1. Following a previous break-off, a sheet cavity starts to grow.
2. At a certain length the growth will cease and a strong re-entrant jet is formed at the closure of the cavity.
3. The velocity of the jet is directed towards the leading edge and of the order of the free stream velocity.
4. The re-entrant jet reaches the cavity near the leading edge and impinges on the cavity interface.
5. The rear part of the cavity sheet breaks off and transforms into a more or less spanwise cylindrical bubble cloud. The upstream directed momentum of the jet causes a large circulation around the cloud.
6. The front part of the original cavity is reduced to a tiny sheet cavity, which will grow again and the cycle starts all over. The cloud is transported downstream.

This paper concentrates on the numerical modelling of stages 1-4 of the unsteady shedding of the 2D cavity sheet. A boundary element method (BEM) is used.

II ■ ANALYSIS

Assuming irrotational, inviscid and incompressible flow, the velocity field \vec{v} can be derived from a potential Φ , satisfying :

$$\nabla^2 \Phi = 0 \text{ with } \vec{v} = \nabla \Phi \quad (1)$$

The potential is split into two parts :

$$\Phi(\vec{x}, t) = \Phi_{\infty}(\vec{x}) + \varphi(\vec{x}, t) \quad (2)$$

representing the main flow $\Phi_{\infty}(\vec{x}) = \vec{U}_{\infty} \cdot \vec{x}$, respectively the disturbance flow φ with $\vec{w} = \nabla \varphi$, which must vanish at infinity : $\vec{w}(\vec{x} \rightarrow \infty, t) \rightarrow 0$. On the wetted parts of the profile impermeability requires

$$\frac{\partial \varphi}{\partial n} = -\vec{U}_{\infty} \cdot \vec{n} \quad (3)$$

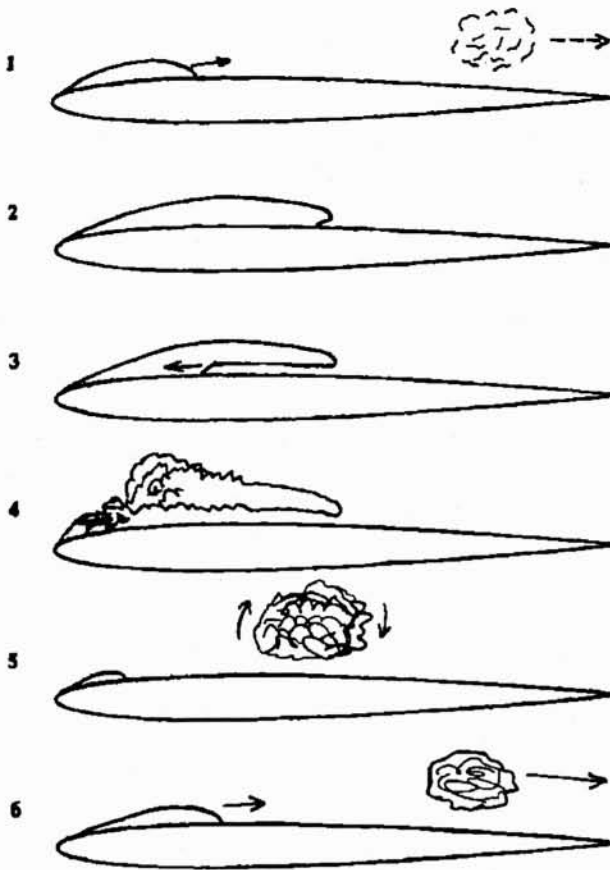
On the cavity surface, described by $F(x, t) = 0$, the kinematic and the dynamic boundary conditions must be satisfied. The kinematic boundary condition can be written, after

normalisation with $\bar{F} = \frac{F}{|\nabla F|}$ and $\frac{\nabla F}{|\nabla F|} = \vec{n}$,

$$\frac{D\bar{F}}{Dt} = \frac{\partial \bar{F}}{\partial t} + \vec{u} \cdot \vec{n} = 0 \quad (4)$$

Modélisation numérique 2D des poches de cavitation instationnaires

Une méthode des éléments aux frontières a permis de modéliser en 2D les poches de cavitation instationnaires. Des polynômes du 3^e degré sont utilisés pour représenter des quantités telles que le potentiel sur la partie mouillée du profil, la vitesse normale sur la poche, la géométrie du profil et la poche. La poche se développant, le jet rentrant et le comportement de la poche près du point de fermeture ont été calculés et les résultats s'accordent qualitativement avec les résultats expérimentaux.



1. Schematic cloud break-off cycle.

Alternatively, the free surface can also be considered as an infinite set of the same material particles, of which the location $\vec{x}_f(t)$ is given by :

$$\frac{Dx_f}{Dt} = \nabla \Phi \tag{5}$$

Physically, equation (4) describes the displacement of a point on the free surface in the direction normal to the free surface, for which only the normal velocity is needed. In equation (5) in addition the tangential velocity is used to determine the position of the free surface.

Over a free surface a jump in the tangential velocity exists, so formally it is not correct to speak of either particles or a material velocity of the free surface. The choice of the tangential velocity is arbitrary, immaterial so to say, since it gives no contribution to the displacement of a non-material interface. Analytically the formulations (4) and (5) are equivalent. However, for numerical modelling they are not equivalent.

If we assume thermodynamic equilibrium and no gas, but only vapour inside the cavity, the dynamic boundary condition states, that on the cavity interface the pressure is equal to the vapour pressure p_v :

$$p = p_v = p_\infty - \frac{1}{2} \rho U_\infty^2 \sigma \text{ with } \sigma = \frac{p_\infty - p_v}{\frac{1}{2} \rho U_\infty^2} \tag{6}$$

In potential flow this pressure p_v can be substituted in Bernoulli's equation :

$$\frac{\partial \phi}{\partial t} + \frac{1}{2} (U_\infty^2 + 2\vec{U}_\infty \cdot \nabla \phi + |\nabla \phi|^2) = \frac{1}{2} U_\infty^2 (1 + \sigma) + \vec{g} \cdot \vec{x} \tag{7}$$



2. HSV observations of the break-off cycle.

where a reference pressure p_∞ has been taken at $\vec{x}_\infty = 0$.

For a point moving with arbitrary velocity \vec{v}_* the rate of change of ϕ is :

$$\frac{d\phi}{dt} = \left(\frac{\partial}{\partial t} + \vec{v}_* \cdot \nabla \right) \phi = \frac{1}{2} (U_\infty^2 (1 + \sigma) - |\nabla \phi|^2 + 2 \vec{v}_* \cdot \nabla \phi) + \vec{g} \cdot \vec{x} \tag{8}$$

For a material point the velocity \vec{v}_* is equal to $\nabla \Phi$ and the time derivative is the material derivative $\frac{D}{Dt}$:

$$\frac{D\phi}{Dt} = \frac{1}{2} (U_\infty^2 \sigma + |\nabla \phi|^2) + \vec{g} \cdot \vec{x} \tag{9}$$

After performing the time integration of (9) a new value for ϕ is obtained, which can be used as a Dirichlet-type condition on the cavity boundary.

Since in 2D the flow domain around a hydrofoil is not simple connected, the solution for the Laplace equation for the potential is non-unique. However, it can be made unique by imposing the Kutta condition.

III ■ NUMERICAL MODELLING

● 3.1 Matrix equation

The solution of the Laplace equation (1) can formally be written as :

$$\beta \phi(\vec{x}_p) = \int_S \frac{\partial}{\partial n} (\phi(\vec{x}_n)) G(\vec{x}_n; \vec{x}_p) ds - \int_S \phi(\vec{x}_s) \frac{\partial}{\partial n} (G(\vec{x}_s; \vec{x}_p)) ds \tag{10}$$

where S is the boundary of the simple connected computational domain. For interior points β is equal to 1, however on the boundary $\beta = \frac{\theta}{2\pi}$, with θ the angle between the right and left tangent to the boundary. So on the smooth part of the boundary $\beta = \frac{1}{2}$, whereas at the sharp trailing edge $\beta = \frac{2\pi - \theta_{TE}}{2\pi}$, with θ_{TE} the wedge angle at the trailing edge.

Green's function $G(\vec{x}_s, \vec{x}_p) = \frac{1}{2\pi} \log|\vec{x}_s - \vec{x}_p|$ is the standard solution.

The potential $\varphi(\vec{x}_p)$ in a general point \vec{x}_p can be expressed in the values of φ and $\frac{\partial\varphi}{\partial n}$ on the boundary S by using (10). On the profile $\frac{\partial\varphi}{\partial n}$ is prescribed according to (3), whereas on the cavity interface the potential φ is prescribed, after performing the time integration of (9). By taking \vec{x}_p at the boundary in (10), the unknown φ or $\frac{\partial\varphi}{\partial n}$ can be solved on the profile or the cavity, respectively. This is performed numerically by solving a linear matrix equation :

$$[\mathbf{A}] [\mathbf{q}] = [\mathbf{b}] \quad (11)$$

The vector $[\mathbf{q}]$ consists out of those discrete values of φ or $\frac{\partial\varphi}{\partial n}$ on S , which are unknown. The matrix $[\mathbf{A}]$ is a full non-symmetric matrix, of which the elements represent the contribution of the integral with the unknown quantity. For the φ -part in $[\mathbf{q}]$ the lefthand side of (10) is included in $[\mathbf{A}]$. The vector $[\mathbf{b}]$ contains the contribution of the integral with the known quantity. For the solution of (11) a method devised by Oguz and Prosperetti [4] has been adapted and extended.

3.2 Spatial integration

To compute the integrals in (10) the variables φ and $\frac{\partial\varphi}{\partial n}$, as well as the geometry of the cavity and the profile, are approximated by a third-order polynomial. The cubic is defined in the interval $[x_{i-1}, x_i]$ as :

$$\tilde{y}_i(x) = sy_i + (1-s)y_{i-1} + h_i s(1-s)[(k_{i-1} - d_i)(1-s) - (k_i - d_i)s] \quad (12)$$

with $i = (1, 2, 3, \dots, m)$, where we define :

$$h_i = x_i - x_{i-1}; d_i = \frac{y_i - y_{i-1}}{h_i}; s_i = \frac{x_i - x_{i-1}}{x_i} \text{ for } x \in [x_{i-1}, x_i] \quad (13)$$

These definitions ensure in the nodal points x_i continuity of the function $\tilde{y}_i(x)$ and its first derivative $\tilde{y}'_i(x) (= k_i)$, but not of its second derivative $\tilde{y}''_i(x)$. In early attempts with a cubic spline, where k_i is found by requiring continuity of $\tilde{y}''_i(x)$ in x_i , the solution was sometimes badly deteriorated by occurrence of spline oscillations. Defining k_i instead by averaging the linear slopes, smoothes these oscillations :

$$k_i = \frac{1}{2} (d_i + d_{i-1}) \quad (14)$$

The integrals in (10) are formally represented by

$$\int q(\vec{x}_s) H(\vec{x}_s; \vec{x}_p) ds \quad (15)$$

where q is either φ or $\frac{\partial\varphi}{\partial n}$ and H is either $\frac{\partial G}{\partial n}$ or G . On

each interval $[x_p, x_{i+1}]$ a Gauss-Legendre integration

$$\int_{x_i}^{x_{i+1}} q(\vec{x}_s) H(\vec{x}_s; \vec{x}_p) ds \approx \sum_{j=0}^z \tilde{q}_{ij} H_j w_j \Delta s \quad (16)$$

is applied. The values of \tilde{q}_{ij} and H_j are to be evaluated from the cubics at the $(z+1)$ specific integration points in the interval, of which the abscissa and weights w_j can be found in standard literature ([5]). However, when $q(\vec{x}_s)$ in (16) is the unknown function, then there is no cubic $\tilde{q}_i(\vec{x}_s)$ available to compute q_{ij} . Within one time step that can be solved iteratively :

$$\int_{x_i}^{x_{i+1}} \tilde{q}(\vec{x}_s) H(\vec{x}_s; \vec{x}_p) ds = \int_{x_i}^{x_{i+1}} \hat{q}(\vec{x}_s) H(\vec{x}_s; \vec{x}_p) ds + \int_{x_i}^{x_{i+1}} \tilde{q}(\vec{x}_s) H(\vec{x}_s; \vec{x}_p) ds \quad (17)$$

where $\hat{q} = \tilde{q} - \bar{q}$ is the difference between the cubic approximation \tilde{q} and a piecewise linear function \bar{q} . The linear approximation \bar{q} can be used to obtain the lefthand side of (11). The correction $\hat{q}|_{iter} = (\tilde{q} - \bar{q})|_{iter} \approx \hat{q}|_{iter-1}$ can be used in the third integral in (17) and added to the known terms in $[\mathbf{b}]$.

3.3 Time integration

The time integration is done iteratively. In the first iteration of a time step the values of the various unknown quantities are taken at $t - \Delta t$. In the subsequent iterations, the time integration is centered around $t - \frac{\Delta t}{2}$:

$$X_i|_t^{iter} = X_i|_{t-\Delta t} + \frac{\Delta t}{2} (VX|_t^{iter-1} + VX|_{t-\Delta t}), \text{ idem for } Y_i|_t^{iter} \quad (18)$$

$$\Phi_i|_t^{iter} = \Phi_i|_{t-\Delta t} + \frac{\Delta t}{2} (D\Phi|_t^{iter-1} + D\Phi|_{t-\Delta t}) \quad (19)$$

with the discrete material derivative $D\Phi$ according to (9), gravity being neglected and $|\nabla\Phi|^2 = WN^2 + WS^2$, with WN and WS the components of the disturbance velocity.

To prevent instabilities a relaxation of the displacement and Φ is applied after each iteration, e.g. :

$$(X_i|_t^{iter})_{relax} = k_{relax} X_i|_t^{iter} + (1 - k_{relax}) X_i|_t^{iter-1} \text{ with } k_{relax} = 0,5 \quad (20)$$

The calculations are initialized from a fully wetted flow. For time $t > 0$ a stepwise pressure reduction to the prescribed σ -value is introduced. The initial cavity is taken to be short and coincident with the profile.

3.4 Kutta condition

The flow domain around a 2-dimensional foil is not simple connected, hence the Kutta condition is necessary to determine a unique solution, and a cut is made from the profile to infinity, the so-called wake line, making the domain simple connected.

In an unsteady flow the circulation Γ around the profile changes, resulting in a vortex distribution $\gamma(s, t)$ being convected along the wake line :

$$\frac{d\Gamma}{dt} = \frac{d[\Phi]_{TE}}{dt} = \hat{v}_s|_{TE} \gamma|_{TE} \quad (21)$$

where $\bar{v}_s = \frac{1}{2}(v_s^+ + v_s^-)$ is the average of the tangential velocities on both sides of the vortex wake at the trailing edge. The strength of the local vortex distribution $\gamma(s)$:

$$\gamma(s) = \frac{\partial [\Phi(s)]}{\partial s} \tag{22}$$

This implies that the tangential velocity is discontinuous over the wake line. The wake line starts at the trailing edge and extends downstream to infinity, its position being determined by the kinematic condition (4).

To simplify the calculations the vorticity in the wake is neglected, hence the steady Kutta condition is used :

$$\frac{\partial \Phi^+}{\partial s} = -\frac{\partial \Phi^-}{\partial s} \rightarrow \frac{\varphi_{TE}^{Up} - \varphi_{TE+1}^{Up}}{\Delta s^{Up}} - \frac{\varphi_{TE}^{Low} - \varphi_{TE-1}^{Low}}{\Delta s^{Low}} = U_{sTE}^{Up} + U_{sTE}^{Low} \tag{23}$$

where the tangential direction is counterclockwise along the profile and U_s is the local tangential component of the uniform velocity field U_∞ (fig. 5). In the quasi-steady model there is a constant potential $[\Phi]$ over the wake line, which is equal to the circulation :

$$\Gamma = [\Phi] = \varphi_{TE}^{Low} + \varphi_{TE}^{Up}$$

Velocities are continuous over the wake line, hence its location is arbitrary.

The integrals $\int G \frac{\partial \varphi}{\partial n} ds$ over the upper and lower part of the wake line cancel, since the normal derivatives have opposite sign. The remaining integrals $\int \varphi \frac{\partial G}{\partial n} ds$ give a net contribution of $\int \Gamma \frac{\partial G}{\partial n} ds$. Since the spatial constant doublet distribution along a curve is equivalent to the contribution of two vortices in the end points of that curve, this integral can easily be calculated analytically. One of these vortices is at infinity and hence gives a vanishing contribution to the flow at a finite distance from the profile.

● 3.5 Regriding technique

In the determination of the integrals in (10) the number and distribution of nodal points s_i is not kept constant. For fully wet flow calculations a sine-spacing is applied. For cavitating flow the lower, noncavitating, part of the profile has the same sine-spacing constant fixed in time. On the upper part, the last 10 % is spaced symmetric with the lower part. The cavity part and the first 10 % immediately behind the most rear part of the cavity are spaced equidistant. On the remaining upper part the spacing is relatively coarse in the middle and matches with the spacings in the adjoining regions.

The calculation of the time dependent position of the free surface by tracking of the nodal points, see (18), would result in a very dense distribution of nodal points on the downstream part of the interface. A regridding process is applied after each time step [1]. At odd time steps in the regridding process the grid points are redistributed equidistant over the cavity interface with prescribed distance, adding or removing a point if necessary. At even time steps one discrete point is added and the new location of each discrete point is chosen between two previous discrete points. The alternating grid positions effectively suppress point to point wiggles. After the redistribution of the points over the free surface, the function values at the new locations are calculated, using the cubic function approximations, which were fitted previously using the old distribution. This regridding is considered to be vital for the success of Oğuz's method [4].

● 3.6 Treatment of end points

The detachment point *DP* and the closure point *CP* offer special problems. Each of these points consists actually out of two coinciding discrete points : one on the solid wall (*W*) and the other on the cavity surface (*C*). Hence, in *CP* we have the four relevant function values $\varphi_{CP}^W, \varphi_{CP}^C, WN_{CP}^W$ and WN_{CP}^C , which must be matched somehow. Here *C* and *W* denote values on the cavity respectively the wall. Also the displacement of the end points offers problems. Points on the free surface are transported as material points. In addition, both end points have to remain on the surface of the profile. However, if the detachment point *DP* is moved as a material point, then it will continue to move downstream, owing to the large downstream velocity tangent to the wall. This is not in agreement with reality, where the position of *DP* is observed to be almost steady. This is solved by keeping the location of *DP* fixed in time at the point of minimum pressure found on the fully wetted profile. To ensure continuity of the potential in *DP*, the potential at the cavity border point φ_{CP}^C is prescribed to be the most recent iterated

potential viewed from the profile : $\varphi_{DP}^C|_t^{iter} = \varphi_{DP}^W|_t^{iter-1}$. The

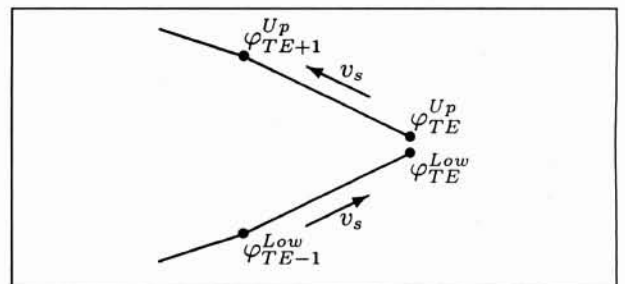
Brillouin-Villat criterium is invoked at *DP*, stating that the curvature of the free surface must be continuous, so the *WN*'s offer no problem. The modelling of *CP* is more critical. In general the cavity will intersect the profile at an angle θ_{CP} with $0 < \theta_{CP} < \pi$, so there are two distinct normal directions. On the profile at *CP* the usual Neumann condition (3) can be applied. On the cavity at *CP* there is a direct relation between the normal velocity on the free surface and the normal and tangential velocities at *CP* on the profile. The potential φ_{CP}^W is determined as solution from the Laplace equation. The potential φ_{CP}^C is calculated using the dynamic boundary condition (8). For a general point on the cavity the material derivative is used, see eq. (9). However, for the *CP* on the cavity that can be different, since the displacement of *CP* must be kept within bounds. To prevent the free surface from sinking into the profile, the displacement of *CP* is corrected only if $\kappa(\theta_{CP} - \frac{1}{2}\pi) < 0$, where κ is the local curvature of the cavity. Then the displacement of the *CP* is as :

$$X_{CP}|_t = X_{CP}|_{t-1} + VX\Delta t + \frac{\Delta s}{c} \left(\theta_{CP}^{W \rightarrow C} - \frac{\pi}{2} \right) \tag{24}$$

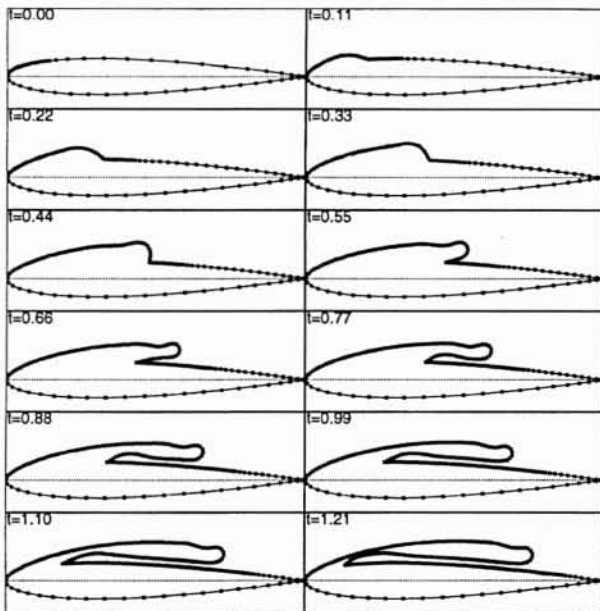
where Δs is the interval size on the cavity and *c* is a large arbitrary constant in the range $c = 50 \dots 500$. Due to the correction term in (24), the displacement no longer matches exactly the calculated velocity, so the general time derivative as in (8) must be applied.

To enforce the theoretically required equality of the potentials φ_{CP}^C and φ_{CP}^W a weighted coupling is applies :

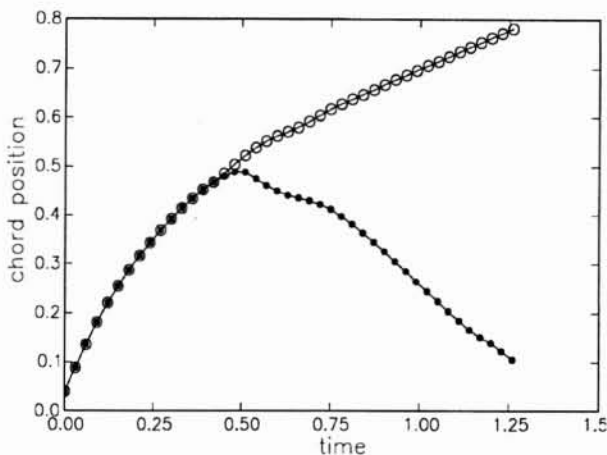
$$\varphi^C|_t = \lambda \varphi^C|_{t-1} + (1 - \lambda) \varphi^W|_{t-1} + \frac{\Delta t}{2} (U_\infty^2(1 + \sigma) - VS^2 - VN^2) + WS(X_{CP}|_t - X_{CP}|_{t-1}) \tag{25}$$



3. The region and some notations around the trailing edge.



4. Cavity growth.



5. The location of the closure point [●] and the maximum cavity length [○].

where the value of $\lambda = 0.9$ is chosen and again the velocities are evaluated at $t - 1$ for the first iteration and at $t - \frac{1}{2}$ for the next iterations. The treatment of the end points which is described here, is a provisional method, which needs further investigation.

IV ■ RESULTS

● 4.1 Wet flow test calculations

Large parts of the procedure can be tested for a fully wetted flow around a Kármán-Trefftz profile with a wedge-shaped trailing edge. Since the analytical solution is known for that profile, it is well suited for testing the program. Tests showed that in the Gauss-Legendre integration (16) the number

of integration points between two nodal points s_i is crucial: 6 integration points resulted in a 10 % error in the circulation, whereas 15 points improved the accuracy to 0.1 %. Both results at the same number of nodal points s_i of $N_p = 100$. The accuracy in the circulation is almost proportional to N_p^{-1} . The required number of nodal points proved to be dependent on the mesh refinement and on the wedge angle at the trailing edge. The close proximity of the elements at the trailing edge causes a strong mutual influence between the elements and hence ill-conditioning. An accurate determination of the influence coefficients in the matrix [A] obviously becomes vital. Additional testing in fully wetted flow has been performed [1].

● 4.2 Tests with a cavity

The initial testing of computations at cavitating flow condition was done with a NACA 0012 profile at an angle of attack $\alpha = 6^\circ$ and a cavitation number $\sigma = 0.25$. This low value of σ would in reality give supercavitation, but in the initial tests calculations usually were aborted when the cavity length had grown to an extent of less than 50 % chord length. Runs are started with about 60 points, of which 25 are on the bottom surface, 30 on the top surface behind the cavity and 5 (including the end points) on the cavity. The initially very small cavity starts with DP and CP at 1 % and 4 % chord respectively.

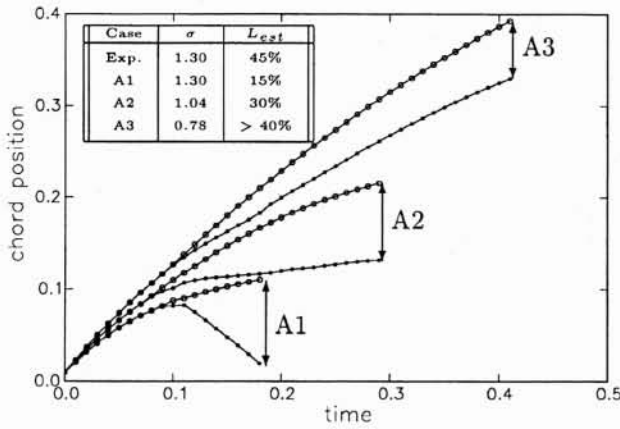
During the computation the number of points on the cavity and the top surface are altered, with a major increase in total number of points when the jet is formed and moves upstream inside the cavity. The most critical aspect of the program is the modelling of the closure point, especially in the phase when the re-entrant jet starts to form. To suppress fatal oscillations, which were initially caused by the use of cubic splines, it proved to be necessary to introduce the smoothing using (14). The development of the cavity is shown in figure 3. Just before the downstream end of the cavity a typical deformation is seen: a dip, followed by an increase in height in the final highly curved, almost circular, end of the cavity. This dip is already found at quite an early stage of the development of the sheet and probably caused by the initial condition. On the initial cavity surface the wet flow solution gives pressures below the prescribed vapour pressure and hence velocities larger than the maximum speed resulting from the steady Bernoulli equation. This effect keeps playing a role during the subsequent evolution of the cavity.

The displacement of the sheet is related to the material velocities. At the cavity end there is a large tangential velocity. The time integration with a finite Δt tends to increase the local radius of the cavity end.

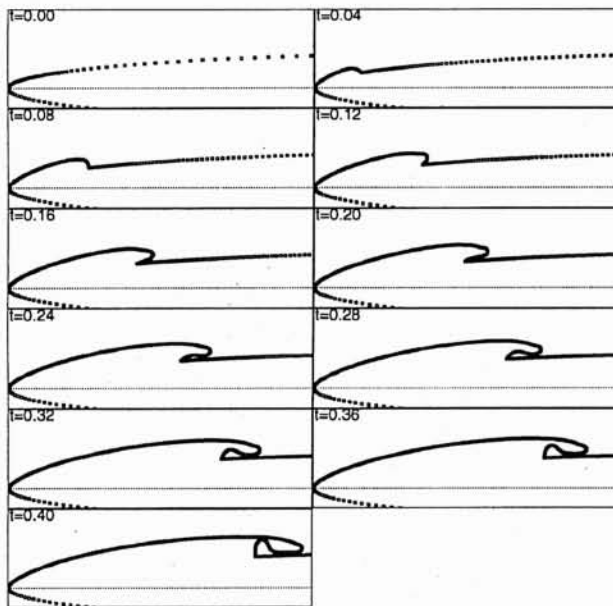
● 4.3 Case A

Also a number of calculations were performed with a NACA 16-009 profile at 4° angle of attack and with $\sigma = 1.3$, since extensive experimental results for that situation had been obtained by de Lange [1]. The computations have been performed for three different values of σ , see table in figure 6. Using the same value $\sigma = 1.3$ as in the experiment resulted in a cavity length which is much too short. In the experiment the actual pressure in the cavity can be larger than the vapour pressure (partial gas pressure, surface tension), so comparison with a lower theoretical σ -value makes sense. Also blockage in the experiment lowers the pressure. Hence, the calculations have been repeated at $\sigma = 1.04$ and $\sigma = 0.78$.

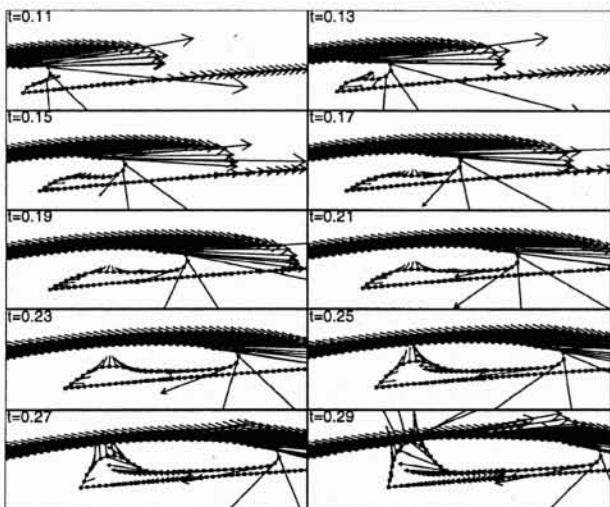
Decreasing σ results in a larger cavity, both in length and thickness, as can be expected. The formation of the jet starts



6. Case A. The location of the closure point [●] and the maximum cavity length [○].



7. Case A3. Cavity growth on region $0 < x < 0.4$, with $\sigma = 0.78$.



8. Case A2. Close-up of cavity growth and jet formation.

at a rather early stage, while the cavity is still rapidly growing. The jet velocity can initially even be directed downstream see *fig. 8*, where the velocity vectors at the surface are shown. After the initial jet formation with a low or in this case even a downstream velocity, the re-entrant jet gains in strength and a high-speed layer is formed. This layer collides with the slow or stagnant front part of the jet and is pushed upwards. When the jet touches the upper cavity interface, the computation is stopped in the present version of the program. This push-up can also be observed experimentally as the frothy cavity surface travelling upstream.

From *figure 6* it is obvious, that the maximum cavity length has not yet been reached, when the calculation aborts. In all cases a decrease in the growth rate is noted with increasing length. A rough estimate of the final cavity length can be found by extrapolation, see table in *figure 6*.

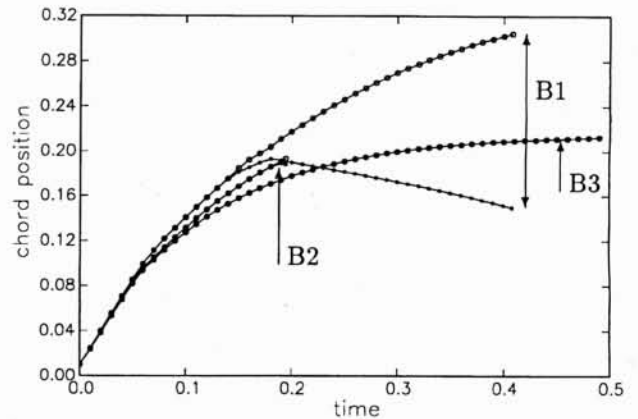
● 4.4 Case B

A final series of computations have been made on a NACA 0012 profile and are compared with experiments of Shen & Petersen [6] on a modified Joukowski profile or with steady numerical computations by van Houten [7], Buist [8] and Uhlman [9], who used either NACA 16-012 or a modified Joukowski profile. In all cases B the cavity is very thin. In case B1 a low speed jet and an upward moving front of the jet is formed, similar as in case A2. In case B2 the angle between the profile and the cavity at CP becomes too small

	$L_c = 40\%$ $\alpha = 4.3^\circ$	$L_c = 30\%$ $\alpha = 4.3^\circ$	$L_c = 25\%$ $\alpha = 3.8^\circ$
Shen & Peterson	$\sigma = 1.13$	$\sigma = 1.21$	$\sigma = 1.13$
Van Houten	$\sigma = 1.37$	$\sigma = 1.53$	$\sigma = 1.51$
Buist	$\sigma = 1.14$	$\sigma = 1.22$	$\sigma = 1.14$
Uhlman	$\sigma = 1.11$	$\sigma = 1.20$	$\sigma = 1.14$

Present method	case B1	case B2	case B3
prescribed	$\sigma = 1.13$ $\alpha = 4.3^\circ$	$\sigma = 1.21$ $\alpha = 4.3^\circ$	$\sigma = 1.13$ $\alpha = 3.8^\circ$
extrapol. result	$L_c = 35\%$	$L_c = 26\%$	$L_c = 21\%$

9. The parameters and results of series B with NACA 0012 profile.



10. Case B. The location of the closure point [●] and the maximum cavity length [○].

and the computation is aborted. In case B3 the coarseness of the grid does not allow the formation of a jet and the calculated shape evolves into a stationary shape. The computational results, though systematically with a shorter cavity length than Shen & Petersen [6], are not unrealistic. The present calculations, series B, are obtained with a NACA 0012 profile, which has a considerably larger nose radius thickness in the region, where the sheet cavity is formed. This reduces the cavity thickness and its length.

● 4.5 Time scales

For the various cases the numerically simulated sheet and jet formation takes about $\frac{1}{3}$ of the total period, which is experimentally observed to be $Str \approx 0.3$, where Str is the dimensionless shedding frequency. This is a reasonable result, considering that the numerical result covers only the first part of a complete shedding cycle.

V ■ CONCLUSIONS

The developed method of calculation gives promising results in 2D, both qualitatively and quantitatively. Further investigation is needed to increase the general robustness of the method, the treatment of the closure point CP , the possible effects of releasing the position of the detachment point DP , improvement of the implementation of the unsteady Kutta condition. etc. Extensions to situations with a fully detached cavity are necessary to study the shedding process. For an accurate determination of the relationship between the Strouhal number and the cavitation number σ a complete cycle must be calculated and not only the first part of the cycle when the cavity is growing. The circulation around such a detached cavity can be quite large, necessitating the proper implementation of the unsteady Kutta condition.

ACKNOWLEDGEMENT

This study is supported by FOM (Foundation for Fundamental Research on Matter) and MARIN (Maritime Research Institute Netherlands).

REFERENCES

- [1] DE LANGE D.F. (1996). — Observation and Modelling of Cloud Formation Behind a Sheet Cavity, PhD-thesis, Univ. of Twente.
- [2] DE LANGE D.F., DE BRUIN G.J., VAN WIJNGAARDEN L. (1993). — Observations of Cloud Cavitation on a Stationary 2D Profile, Proc. IUTAM Symposium : Bubble Dynamics and Interface Phenomena, ed. J.R. Blake e.a., Birmingham.
- [3] LE Q., FRANC J.P., MICHEL J.M (1993). — Partial Cavities : Global Behaviour and Mean Pressure Distribution, J. Fluids Eng., 115, pp. 243-248.
- [4] OGUZ H.N., PROSPERETTI A. (1993). — Dynamics of Bubble Growth and Detachment from a Needle, J. of Fluid Mech., 257, pp. 111-145.
- [5] ABRAMOWITZ M., STEGUN I.A. (1964). — Handbook of Mathematical Functions, Applied Mathematics Series, vol. 55, Washington.
- [6] SHEN Y.T., PETERSON F.B. (1978). — Unsteady Cavitation on an Oscillating Hydrofoil, Proc. 12th Symposium on Naval Hydrodynamics. Washington.
- [7] VAN HOUTEN R.J. (1982). — The Numerical Prediction of Unsteady Sheet Cavitation on High Aspect Ratio Hydrofoils, Proc. 14th Symp. Naval Hydrod., pp. 733-784.
- [8] BUIST J. (1991). — On the Origin and Behaviour of Cavitation Clouds, PhD-thesis, University of Twente.
- [9] UHLMAN J.S. (1987). — The Surface Singularity Method Applied to Partially Cavitating Hydrofoils, J. Ship Res., 31, pp. 107-124.